RSC Advances

PAPER

View Article Online
View Journal | View Issue

Cite this: *RSC Adv.*, 2016, **6**, 72836

Hollow-structured upconverting sesquioxide targeted nanoprobes for magnetic resonance and fluorescence combined imaging†

Jinchang Yin,[a] Chaorui Li,[a] Yubiao Yang,[b] Wenyong Hu,[a] Huan Liu[a] and Yuanzhi Shao*[a]

Received 20th May 2016
Accepted 22nd July 2016

DOI: 10.1039/c6ra13180h

www.rsc.org/advances

Herein, hollow-structured Gd_2O_3 : RE^{3+}/Yb^{3+} (RE = Er, Ho, Tm) nanoparticles (NPs) were prepared *via* a urea-based chemical coprecipitation method followed by subsequent calcination and etching. Under 980 nm near-infrared (NIR) irradiation, upconversion (UC) emission gains the highest intensity of red, green and blue peaks for Gd_2O_3 : Er^{3+}/Yb^{3+}, Gd_2O_3 : Ho^{3+}/Yb^{3+} and Gd_2O_3 : Tm^{3+}/Yb^{3+} NPs respectively. The corresponding fluorescence in-cell images exhibit bright visible light. The continuous color-tunable UC emission of each spectrum was investigated by increasing the concentration of the sensitizer Yb^{3+} ions from 0 to 20 mol% with the most intense red, green and blue emission achieved. The structure, morphology, components and magnetic property of Gd_2O_3 : Ho^{3+}/Yb^{3+} NPs were investigated intensively. The results show that the NPs possess a distinctly hollow structure and uniform spherical shape, and are well-crystallized and highly monodispersed with a mean diameter of 118 nm. Due to the designed hollow structure which is of benefit to water contact of a large number of Gd^{3+} on the surface, the measured T_1 relaxivity of the NPs is nearly 5 times larger than the relaxivity of the commercial gadolinium diethylenetriaminepentaacetate (Gd-DTPA). The relaxation enhancement in the hollow-structured Gd_2O_3 : RE^{3+}/Yb^{3+} (RE = Er, Ho, Tm) NPs is addressed in the framework of Solomon–Bloembergen–Morgan theory. The biocompatibility studies in 293 and HeLa cells indicate that the hollow NPs have no observable cytotoxicity at a concentration up to 200 μg ml^{-1}. All these results demonstrate that the hollow-structured nanocomposite has the potential to be developed into a safe and highly efficient magnetic resonance and fluorescence nanoprobe for in-cell molecular imaging of cancer.

Introduction

Magnetic resonance imaging (MRI), one of the most powerful tools for anatomical images in noninvasive clinical diagnosis techniques is able to acquire 3D tomographic information of soft body tissues.[1] It possesses several significant advantages including high resolution, and low ionizing radiation.[2–4] However, such an imaging technique has a deficiency. When MRI is used to detect cellular activities or extremely slight tissue lesions, it is insensitive and hard to meet increasingly accurate imaging of smaller biological targets.[5–7] It is well-known that, fluorescence imaging (FI) exhibits much higher sensitivity than that of MRI. Therefore, a feasible solution is integration of both MRI and FI to obtain highly desirable resolution and sensitivity.[8–11]

Usually, contrast agents (CAs) which can enhance the contrast between normal and pathological tissues are used in MRI.[12] Traditional paramagnetic Gd^{3+} complex has been demonstrated as thermodynamically stable, water-soluble and non-toxic agents and widely used in clinical MRI. However this powerful commercial agents still have some limitations of relatively low relaxivity, short residence time and non-specificity for targeted imaging inside, particularly outside, the vascular system.[13] Gadolinium oxide (Gd_2O_3) NPs with a high longitudinal relaxivity (r_1) and targeting functionality has been developed as versatile T_1-weighted CAs. This kind particle agents can be internalized into the reticuloendothelial system, produce a characteristic biodistribution and increase the imaging time.[14–17] Ultrasmall Gd_2O_3 nanoparticle colloids display rather high longitudinal relaxitives.[18,19] Luo *et al.*, prepared ligand-free Gd_2O_3-based nanomaterials of around 7.4 nm in the mean size and obtained r_1 value up to 34.26 mM^{-1} S^{-1} on a 3.0 T MRI instrument.[20] Unfortunately, ultrasmall gadolinium oxide (sub-10 nm) could transmigrate the blood–brain barrier and easily

[a]*State Key Laboratory of Optoelectronic Materials and Technologies, School of Physics, Sun Yat-sen University, Guangzhou 510275, P. R. China. E-mail: stssyz@mail.sysu.edu.cn*

[b]*Institute for Advanced Materials, School of Material Science & Engineering, Jiangsu University, Zhenjiang, 212013, P. R. China*

† Electronic supplementary information (ESI) available: SEM and TEM spectra; confocal laser microscopy images. See DOI: 10.1039/c6ra13180h

aggregated, causing *in vivo* intoxication. In the framework of Solomon–Bloembergen–Morgan (SBM) theory,[21–28] we make use of a strategy (Fig. 1) to tailor a hollow structure for fabricating a unique T_1-weighted contrast agent that could expedite water molecules accessing to the hollow region and contacting with Gd^{3+} ions.

The paramagnetic lanthanide ions exhibit a rich variety of magnetic and photoluminescence properties induced by their 4f electrons, which endows materials containing them with much possibility to be developed as ether various high-performance MRI or FI agents or both.[29–32] On the one hand, paramagnetic oxides of Gd^{3+} ions can raise the local relaxation change of the nearby water protons and mainly contribute to bright signals with reducing its longitudinal relaxation time. On the other hand, rare-earth ions (RE^{3+}) with unique luminescent properties based on the excellent host matrix of Gd_2O_3 should not be ignored. Doping appropriate RE^{3+} into Gd_2O_3 nanocrystals can gain the very outstanding photoluminescence.

In recent years, rare-earth nanophosphors including Eu^{3+}, Tb^{3+}, Dy^{3+}-based and upconversion NPs have attracted great attention and shown growing promise in bioimaging as well as semiconductor quantum dots (QDs)[33,34] and organic phosphor molecules.[35–37] Noticeably, organic dyes are subject to the problem of photo-bleaching, an irreversible damage to the molecules arising from the light excitation although they have low toxicity. Quantum dots are blamed for their intrinsic toxicity and chemical instability *in vivo* although they possess good photostability. Compared to organic dyes and QDs, rare-earth-based nanoparticle phosphors have gained great popularity and have been recognized as a new generation of biological optical labels due to their unique luminescent and biocompatible properties, such as large Stokes shift, high photochemical stability, long luminescent lifetime, sharp emission spectra and low toxicity. However, the commonly used single RE^{3+} doped NPs with downconversion luminescence, which is excited by ultraviolet (UV) or visible light, has several deficiencies in bioimaging applications, such as tissue photodamage, scattering, low tissue penetration and strong background autofluorescence.[38] Therefore, designing novel and more effective photoluminescent materials with high-intensity emission of red, green or blue has always been a frontier topic of bioimaging technologies. There is no doubt that UC fluorescence[39,40] excited by the NIR light has been the most promising in-cell FI due to its high tissue penetration, minimal autofluorescence and low photo-damage, which can cover these shortages of the downconversion nanophosphors.

In this study, Er^{3+}/Yb^{3+}, Ho^{3+}/Yb^{3+} and Tm^{3+}/Yb^{3+} functioning as activator/sensitizer have been codoped into the host Gd_2O_3 for yielding the strong UC luminescence, and they present the bright red, green and blue lights. Due to keeping a hollow structure and Gd^{3+} as the dominant composition, the as-formed NPs hold an outstanding MR property. The materials reported in the paper possess the following merits: (1) optimum particle size (approximately 120 nm) for cellular uptake process as well as avoiding transmigrating the blood–brain barrier. (2) Excellent water-solubility, dispersibility and uniformity for biological application. (3) Resulting high longitudinal relaxivity owing to its large surface-to-volume (S/V) ratio of Gd^{3+} ions originated from the unique hollow structure. (4) Superior UC luminescent properties giving rise to the outstanding fluorescence bioimaging. (5) Extremely low cytotoxicity and favorable biocompatibility for utilizing as a promising targeted nanoprobe. What's more, facile and effective synthesis approach with a great potential for large-scale and low-cost production should not be ignored.

Experimental section

Fabrication of hollow Gd_2O_3 : RE^{3+}/Yb^{3+} (RE = Er, Ho, Tm) NPs

Monodisperse silica nanospheres were synthesized by the well-known Stober process as reported,[41] with minor adjustments. This approach was carried out through the hydrolysis of tetraethyl orthosilicate (TEOS) in an ethanol medium in the presence of water and ammonia at a specific molar ratio. Briefly, concentrated ammonium solution (6 ml), ethanol (100 ml) and deionized water (2 ml) were sequentially added into an Erlenmeyer flask, thoroughly stirred and persistently overheated to 40 °C through a stainless steel water-bath heater. Then TEOS solution (3 ml) was added slowly, and the mixtures were stirred moderately at 40 °C for 24 h. The lacteal suspension colloid were isolated by centrifugation at 10 000 rpm for 15 min and ultrasonically washed with deionized water and ethanol three times respectively. The resulting silica NPs were put into twelve tubes

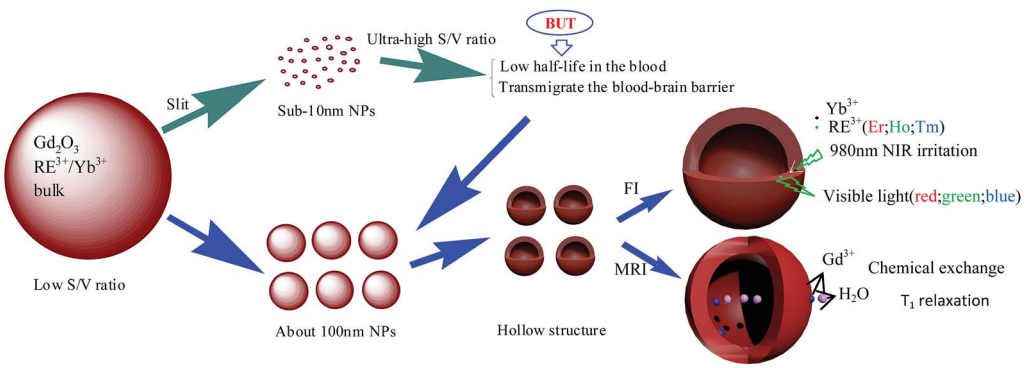

Fig. 1 Schematic illustration of constructing hollow-structured NPs as a high-performance MRI-FI contrast agent.

evenly. Core–shell structured SiO_2@Gd_2O_3 : RE^{3+}/Yb^{3+} (RE = Er, Ho, Tm) NPs were prepared using the following urea-based homogeneous precipitation process according to a previously reported protocol[37,41] with some modifications. Typically, one tube of the as-synthesized SiO_2 NPs was centrifuged and dispersed into an Erlenmeyer flask with 100 ml of deionised water. The flask were put into an ultrasonic cleaning tank for 30 minutes to make sure the nanospheres were dispersed adequately. Then urea (1.0 g) and the appropriate amounts of $RE(NO_3)_3 \cdot 6H_2O$ (RE = Er, Ho, Tm), $Yb(NO_3)_3 \cdot 6H_2O$ and $Gd(NO_3)_3 \cdot 6H_2O$ were dissolved into the above solution. The total amounts of rare earth ions were kept at 0.5 mmol, whereas the relative molar ratio of them was varied in a certain proportion. The mixture was heated at 80 °C under water bath with a vigorous agitation for 2 h. The NPs were thereby successfully encapsulated with gadolinium oxide carbonate hydrate. The precursors were isolated by centrifugation at 8000 rpm for 10 min and collected after washing with deionized water and ethanol, and then dispersed into a small beaker. The dispersions firstly were frozen in a refrigerator and then placed in a vacuum freeze drier at minus 40 °C. The dry powders were heated at 550 °C in an electric furnace for 5 h, leading to the SiO_2@Gd_2O_3 : RE^{3+}/Yb^{3+} (RE = Er, Ho, Tm) NPs. The calcinated powders were dispersed into the sodium hydroxide solution for 24 h and the final Gd_2O_3 : RE^{3+}/Yb^{3+} (RE = Er, Ho, Tm) NPs with a hollow structure were yielded.

Characterization

The morphology of the NPs were inspected using a thermal field emission environmental scanning electron microscope (SEM, FEI Quanta 400F, 30 kV). Transmission electron microscope (TEM, FEI Tecnai-G2 Spirit, 300 kV) was employed to observe the hollow structure of the NPs. High-resolution (HR) TEM images and selected area electron diffraction (SAED) patterns were also obtained by TEM. A histogram of the particle size distribution was acquired by measuring 250 particles in several TEM images. The crystalline structure of the NPs was characterized using an X-ray diffractometer (XRD, D-MAX 2200X VPC, RIGAKU) with a zero background sample holder. The fluorescent excitation and emission spectra of dried powder samples placed on quartz substrates were tested by Edinburgh spectrofluorophotometer (FLS 920) at room temperature, equipped with a 150 W Xenon lamp as the excitation source. Magnetization curves at room temperature and zero field cooling and field cooling curves of NPs were acquired by magnetic property measurement system equipped with superconducting quantum interference device (SQUID, Quantum Design, USA). The RE^{3+} concentrations of Gd_2O_3- : RE^{3+}/Yb^{3+} (RE = Er, Ho, Tm) NPs were determined by inductively coupled plasma atomic emission spectroscopy (ICP-AES, Optima 7300 DV, PerkinElmer).

MR relaxivity measurement

The longitudinal relaxation time measurements of the NPs were performed using a 0.55 T MRI system (MicroMR-18, Shanghai Niumag Corp.). The samples were dispersed in deionized water and kept in a running ultrasonic cleaner for 0.5 h at 40 °C. Several 0.8 ml suspension liquids with various concentrations of gadolinium ions were transferred into a series of numbered small tubes. After injecting 0.2 ml of 2.5 wt% boiling agar solution into each tube, samples with Gd^{3+} ion concentrations varied from 0 to 0.1 mM with a volume of 1.0 ml were prepared for MR relaxation time measurements. The commercial contrast agent Gd-DTPA solutions were fabricated following the similar procedures. The longitudinal relaxation times of water protons in presence of Gd_2O_3 : RE^{3+}/Yb^{3+} (RE = Er, Ho, Tm) NPs at different concentrations were measured with inversion recovery pulse sequences with TR = 2000 ms and TI = 500–2000 ms. The following parameters were adopted in the measurements. IR series: P90 (μs) = 11.00, P180 (μs) = 22.00, SW (kHz) = 50, RG1 = 18, RG2 = 3, NS = 4, sampling number = 36.

Cell culture and live cells confocal microscopy imaging

Human cervical HeLa cell lines were seeded in the wells of 24 well plates and grown in the logarithmic phase at 37 °C under 5% CO_2 in Dulbecco's modified Eagle's medium (DMEM) containing 10% fetal bovine serum (FBS), penicillin(100 units per ml) and streptomycin (100 mg ml^{-1}) overnight. Then the cells were incubated with the Gd_2O_3 : RE^{3+}/Yb^{3+} (RE = Er, Ho, Tm) NPs in a fresh culture media for another 1 h. After this co-incubation period, the cells were washed with phosphate buffer solution (PBS) to remove the excess NPs and dead cells, and then observed under a confocal laser microscopy (Leica TCSSP8) operating at an irritation wavelength of 980 nm.

Cells cytotoxicity assay

The cell viability levels were assessed by using cell counting kit solution (CCK-8) assays. The normal embryonic kidney 293 cells and cervical carcinoma HeLa cells employed to test the cytotoxicity of the Gd_2O_3 : RE^{3+}/Yb^{3+} (RE = Er, Ho, Tm) NPs. A specific number of cells (logarithmic growth phase, 8000 per well) were dropped on 10 mm glass cover slips of 96 well plates at 37 °C under 5% CO_2 in the culture media (DMEM + 10% FBS, 1640 + 10% FBS) for 24 h. Then the cells were incubated with fresh culture media containing different Gd^{3+} + Yb^{3+} + RE^{3+} concentrations of Gd_2O_3 : RE^{3+}/Yb^{3+} (RE = Er, Ho, Tm) NPs and regarded with pure culture media without any nanoparticles as negative control. After further co-incubating for 48 h, 10 μl of the CCK-8 colorimetric solution was added into each well. And the cells were cultured for another 2 h at 37 °C under 5% CO_2. Then all the culture media were removed and the absorbance of each well at 450 nm was measured on a microplate reader as a blank value OD_{blank}. Finally, the culture media with the soluble formazan were directly quantified by measuring the absorbance as a sample value OD_{sample}. The optical absorbance at a wavelength of 450 nm was measured by an enzyme-linked immunosorbent assay using a MultiskanMK3 microplate photometer (Thermo, scientific, Waltham). Three independent repetitions of the detection were

carried out to acquire the final optical density (OD) values and the standard deviation values.

Results and discussion

Synthesis and fluorescence properties of hollow Gd_2O_3 : RE^{3+}/Yb^{3+} (RE = Er, Ho, Tm) NPs

In the present study, amorphous $Gd_2O(CO_3)_2 \cdot nH_2O$ NPs substituted RE^{3+} for a few Gd^{3+} cations were encapsulated onto the surface of the silica nanosphere by urea-based coprecipitation process with further calcinating and etching to form hollow-structured Gd_2O_3 : RE^{3+}/Yb^{3+} (RE = Er, Ho, Tm) NPs. The synthetic protocol comprises four consecutive steps, schematically represented in Fig. 2. Firstly, monodispersed SiO_2 NPs were fabricated by the Stober approach as the cores for further deposition. Secondly, a uniform $Gd_2O(CO_3)_2 \cdot nH_2O$: RE^{3+}/Yb^{3+} precursor formed by reacting with urea at 80 °C was deposited onto the surfaces of the SiO_2 NPs utilizing a facile homogeneous coprecipitation process. Thirdly, the precursor layer was converted into a Gd_2O_3 : RE^{3+}/Yb^{3+} shell coated on the SiO_2 nanocores by annealing. At last, silica cores were eliminated by NaOH solution to form the hollow NPs.

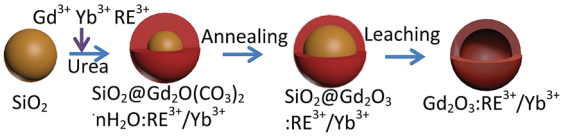

Fig. 2 Scheme of synthetic procedures of hollow Gd_2O_3 : Re^{3+}/Yb^{3+} NPs.

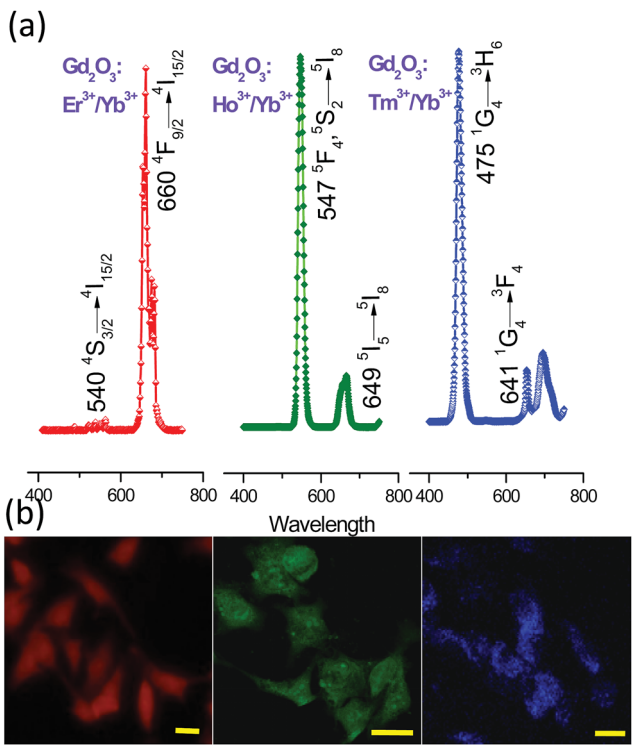

Fig. 3 (a) UC emission spectra, (b) corresponding fluorescence images of hollow-structured Gd_2O_3 : RE^{3+}/Yb^{3+} (RE = Er, Ho, Tm) NPs (scale bar = 25 μm).

Under 980 nm NIR irradiation, UC emission spectra give the highest intensity of red, green and blue peaks for as-calcinated hollow Gd_2O_3 : Er^{3+}/Yb^{3+}, Gd_2O_3 : Ho^{3+}/Yb^{3+} and Gd_2O_3 : Tm^{3+}/Yb^{3+} NPs respectively as shown in Fig. 3(a). Continuous color-tunable UC emission of each spectrum was carried out by increasing the concentration of the sensitizer Yb^{3+} ions from 0 to 20 mol%.

Thus the most intense red, green and blue emission was achieved successfully. The measured optimal stoichiometric molar ratios of Gd^{3+} : RE^{3+} : Yb^{3+} (RE = Er, Ho, Tm) are 88 : 2 : 10, 93 : 2 : 5 and 83 : 2 : 15, respectively. For Gd_2O_3- : Er^{3+}/Yb^{3+} NPs, the prominent bands centered at 540 and 660 nm are assigned to the transitions of Er^{3+} ions from $^4S_{3/2}$ and $^4F_{9/2}$ states to the group state of $^6I_{9/2}$. For Gd_2O_3 : Ho^{3+}/Yb^{3+} NPs, the dominant emission peaks at 547 and 649 nm are assigned to the $^5F_4$,$^5S_2$–$^5I_8$ and $^5I_5$–$^5I_8$ transitions of Ho^{3+}. And for Gd_2O_3- : Tm^{3+}/Yb^{3+} NPs, the main emission peaks are presented at 475 and 641 nm, which can be ascribed to typical f–f transition $^1G_4$–$^3H_6$ and $^1G_4$–$^3F_4$ of Tm^{3+}. The corresponding fluorescence in-cell images exhibit bright visible red, green and blue lights with a irradiation wavelength of 980 nm as shown in Fig. 3(b), suggesting that the NPs synthesized possess excellent UC fluorescence emission properties even though they are swallowed by the cells. These results demonstrate that the visible red, green and blue fluorescence of the NPs are intense enough for in-cell optical imaging and indicate the great potential for bioimaging.

Morphology, structure and composition of the prepared hollow Gd_2O_3 : Ho^{3+}/Yb^{3+} NPs

For investigating the structure, morphology, composition and MR properties of the NPs in detail, we focused on Gd_2O_3 : Ho^{3+}/Yb^{3+} NPs as an example due to their similarity and uniformity. The typical SEM images of the precursor SiO_2@$Gd_2O(CO_3)_2$- $\cdot nH_2O$: Ho^{3+}/Yb^{3+} NPs, the calcinated powder SiO_2@Gd_2O_3- : Ho^{3+}/Yb^{3+} NPs and the etched hollow-structured Gd_2O_3 : Ho^{3+}/Yb^{3+} NPs are displayed in Fig. S1(a–c) in ESI† profiles. It is easily seen that almost all the NPs are spherical and highly monodispersed with a good uniformity.

The representative TEM and STEM images of the as-prepared nanocrystals were shown in Fig. 4(a and b). The particle displays an excellent hollow framework and a spherical shape with a smooth surface. The energy-dispersive X-ray (EDX) element mapping images demonstrate the primary composition of the host material Gd_2O_3. Another rare-earth ions can be detected through photoluminescent emission. Note that the density of the whole O mapping is not homogeneous, dividing into two parts. The density in core part is smaller than that of the shell obviously, demonstrating that the NPs possess a hollow structure rather than a core–shell architecture. The corresponding size distribution histogram (250 recognizable nano-particles were randomly selected from several TEM images) shows that the NPs have a mean diameter of approximately 118 nm and their sizes distributes within the narrow range of 95–135 nm

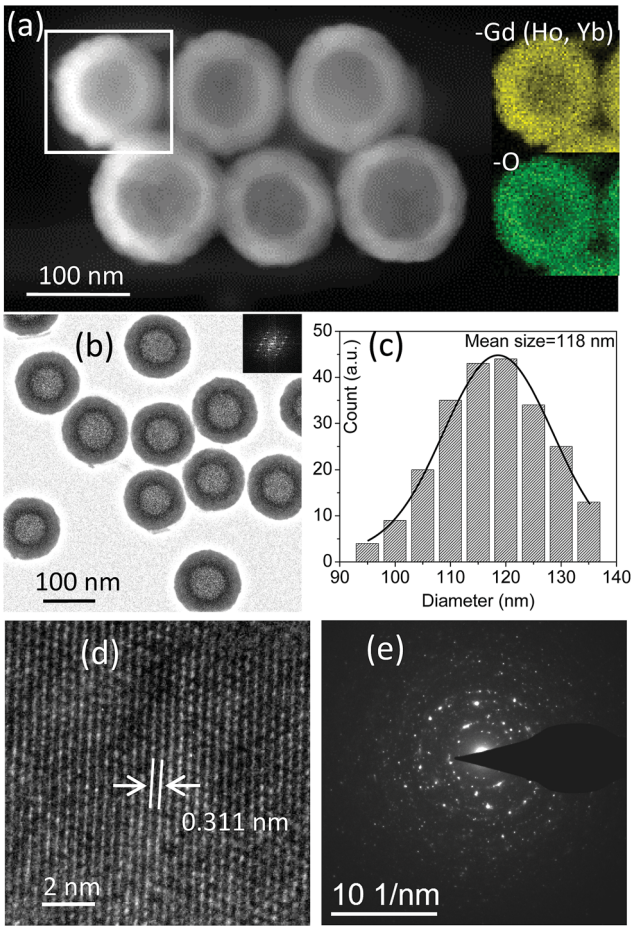

Fig. 4 (a) Scanning TEM image with high angle annular dark field (STEM-HAADF image); inset: EDX mapping image of hollow structured Gd_2O_3 : Ho^{3+}/Yb^{3+} NPs. (b) Typical TEM image; Right upper inset: the related fast Fourier transform. (c) Size distribution histogram derived from several TEM images (250 particles measured) and mean size of 118 nm calculated with Gaussian fitting. (d) HR-TEM image and (e) SAED pattern of the nanocrystal.

(Fig. 4(c)). The following HR-TEM images and SAED pattern (Fig. 4(d and e)) of the NPs are the evidence of the polycrystalline structure and the excellent crystalline nature. The pattern can be simply indexed as cubic Gd_2O_3 with (222) diffraction ring at space interplanar distances of 0.311 as shown in the HR-TEM image, which is in agreement with that of Gd_2O_3 in the database (PDF # 65-3181).

Furthermore, the triplicate TEM images of hollow Gd_2O_3 : Er^{3+}/Yb^{3+}, Gd_2O_3 : Ho^{3+}/Yb^{3+}, Gd_2O_3 : Tm^{3+}/Yb^{3+} NPs and a comparison diagram of the average particle size and shell thickness of each synthesis are shown in Fig. S2(a and c),† also indicating a superior hollow structure with a good uniformity and dispersibility. The crystalline structure of the as-calcinated and etched sample is further identified by X-ray powder diffraction pattern (Fig. 5). It confirms that all the peaks of the XRD patterns match well with that of the cubic Gd_2O_3 (PDF # 65-3181), and no impurity phases were observed. The narrow and strong peaks of XRD also exhibit a good crystallinity, which is consistent with the results acquired from TEM analysis. Note

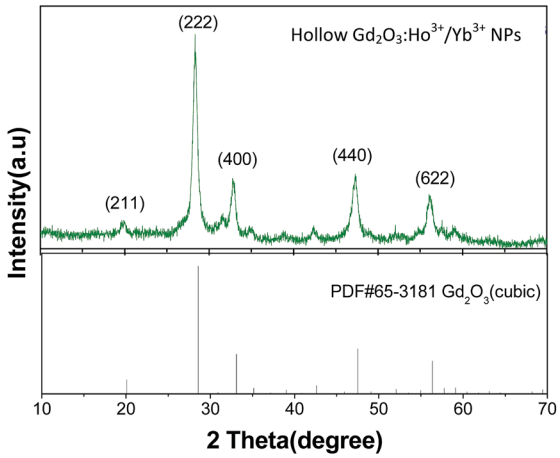

Fig. 5 XRD pattern of the hollow-structured Gd_2O_3 : Ho^{3+}/Yb^{3+} NPs with a standard cubic phase of Gd_2O_3.

that the broadening of the peaks shows small crystalline size of the resultant samples.

Magnetic and relaxation properties of hollow Gd_2O_3 : Ho^{3+}/Yb^{3+} NPs

Zero field cooling (ZFC) and field cooling (FC) *M–T* curves (magnetization *vs.* temperature) in the external magnetic field *H* of 100 Oe and magnetization *M–H* curves at room temperature of hollow-structured Gd_2O_3 : Ho^{3+}/Yb^{3+} NPs are shown in Fig. 6. In the low external magnetic field (H = 100 Oe), ZFC and FC curves are still superposition obviously. The magnetization curve displays the classic characteristics of the paramagnetic materials at room temperature. The magnetic susceptibility (χ) of the NPs was calculated to be 1.8×10^{-4} emu g^{-1} K^{-1}.

Due to the paramagnetic Gd^{3+} ions on the inner and outer surface of hollow Gd_2O_3 : Ho^{3+}/Yb^{3+} NPs, they should be employed as a positive signal enhancement contrast agent on the T_1-weighted MR imaging. The longitudinal relaxivity (r_1) value of the NPs has been evaluated shown in Fig. 7. It is almost five times than that of the traditional commercial Gd-DTPA.

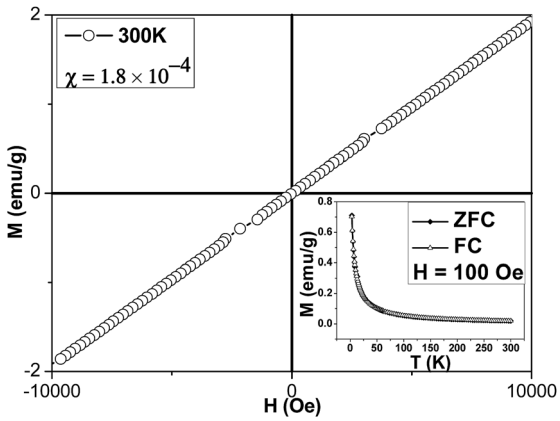

Fig. 6 Room temperature magnetization (*M–H*) curve of Gd_2O_3-: Ho^{3+}/Yb^{3+}.

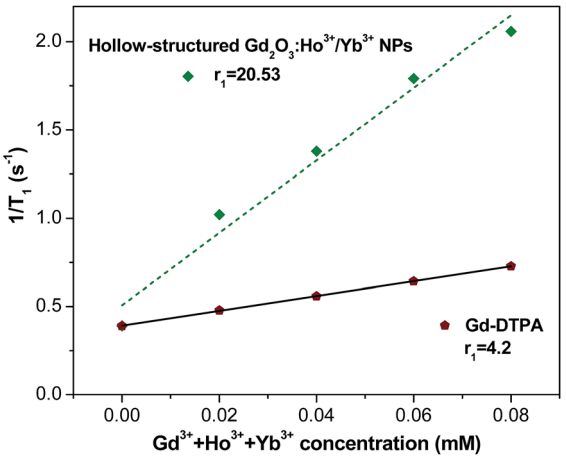

Fig. 7 Plots of $1/T_1$ inverse relaxation times of Gd_2O_3 : Ho^{3+}/Yb^{3+} compared to Gd-DTPA as a function of Gd^{3+} + Ho^{3+} + Yb^{3+} molar concentration.

According to the SBM theory as formulated in eqn (1) and (2), the longitudinal T_1 relaxation rate (R_1) of water nuclear spins in the vicinity of the existing contrast agents is deemed to be distance-dependent with d^{-6}, where d is the distance between the water proton and Gd^{3+} ions.[20–25]

$$R_1 = \frac{1}{T_1} = \frac{qP_m}{T_{1m} + \tau_m} \quad (1)$$

$$\frac{1}{T_{1m}} = \frac{2}{15}\frac{\gamma^2 g^2 \mu_B{}^2 S(S+1)}{d^6}\left[\frac{3\tau_{c1}}{(1+\omega_I{}^2\tau_{c1}{}^2)} + \frac{7\tau_{c1}}{(1+\omega_S{}^2\tau_{c2}{}^2)}\right], \quad (2)$$

where T_{1m} is the T_1 of the water hydrogen contacting to the Gd^{3+} ions, and q is the hydration number, and P_m is the mole fraction of Gd^{3+} ions. τ_m is the residence lifetime of water, and τ_{ci} is the correlation time ($i = 1, 2$). ω_I is the proton Larmor frequency, and ω_S is the angular electronic frequency ($\omega_S = 658\omega_I$). g is the electronic g-factor ($g = 2$), and γ is the gyromagnetic constant for protons (2.675×10^8 T^{-1} s^{-1}), and μ_B is the Bohr magneton (9.274×10^{-24} J T^{-1}) and S is the total electron spins of Gd^{3+} ions.

SBM theory suggests that relaxation rate R_1 declines with distance d drastically. Compared to Gd^{3+} chelated by a huge organic molecule, DTPA, the as-fabricated NPs with Gd^{3+} ions exposing on the surface are ligand-free, leading to a shorter distance, *i.e.* smaller d. Furthermore, the hollow structure is extremely favorable for exposed Gd^{3+} ions contacting with a larger number of waters, *i.e.* larger q, and facilitating much more relaxed water in close rapidly exchanging with Gd^{3+} ions. These water molecules are divided into two parts, namely inner-surface water in the hollow region and outer-surface water as shown in Fig. 1. T_1 contrast enhancement is primarily attributed the chemical exchanges with the Gd^{3+} centers directly in the outer-surface regions. It means that the longitudinal relaxivity (r_1) of the contrast NPs can be improved by increasing the hydration number q of waters that coordinate directly to Gd^{3+} in the both regions. Therefore the NPs synthesized in this study possess a better T_1 contrast enhancement with a higher relaxivity value than that of Gd-DTPA.

For Gd_2O_3-based NPs, another significant factor, surface to volume (S/V) ratio of the NPs has to be considered. Since the longitudinal relaxivity (r_1, s^{-1} mM^{-1}) of the contrast agents depends upon the relaxation rate (R_1, s^{-1}) of surrounding water affected by the effective surface water-contacted Gd^{3+} ions *versus* the Gd^{3+} concentration of the total volume, increasing S/V ratio is the most effective approach to enhance the relaxivity of the contrast agent. And it is just the most significant merit of our constructing hollow-structured NPs. The relationship between the longitudinal relaxivity and Gd^{3+} concentration is interpreted by the following eqn (3):[26]

$$R_1 = \frac{1}{T_1} = \frac{1}{T_{1i}} + r_1[\mathrm{Gd}], \quad (3)$$

where $1/T_{1i}$ is intrinsic solvent relaxation rate in the absent of Gd^{3+} and $1/T_1$ is the observed solvent relaxation rate in the presence of Gd^{3+}. In fact, the main contribution to the longitudinal relaxivity of Gd-based NPs is originated from the exposed Gd^{3+} ions. Therefore, decreasing the interior Gd^{3+} ions can reduce the volume of Gd_2O_3 (V) to a certain extent. And the more the surface water-contacted Gd^{3+} ions are, the larger the hydration number q, which then gives rise to a shorter relaxation time T_1 according to the SBM eqn (1). This unique structure endows the nanocomposites with an extremely high S/V ratio, resulting in an efficient T_1 contrast enhancement. Due to the large hollow core diameter, the proportion of Gd^{3+} in the whole volume is lower whereas in the outer surface it is higher than the counterpart of pure Gd_2O_3 NPs. In our case, a few Re^{3+} ions are doped into the Gd_2O_3 NPs which may decrease r_1 slightly but it is negligible. Contrarily, it can bring a significant fluorescence. Therefore, the as-formed hollow Gd_2O_3 : RE^{3+}/Yb^{3+} (Re = Er, Ho, Tm) NPs exhibit an outstanding magneto-fluorescent property simultaneously, making it serve as a versatile nanoprobe for magnetic resonance and optical imaging.

In-cell optical imaging and cytotoxicity of the as-synthesized hollow Gd_2O_3 : Ho^{3+}/Yb^{3+} NPs

To verify the effectiveness of using the as-fabricated Gd_2O_3 : Ho^{3+}/Yb^{3+} NPs with an optimized Re^{3+} concentrations as potential optical bioimaging probes for cellular studies, we conducted *in vitro* biological experiments using the cervical carcinoma HeLa cells with 20 μg ml^{-1} NPs. After co-incubation for 2 h, the cells were washed and then observed by laser scanning microscope at an excitation wavelength of 980 nm and emission wavelength in green channel which can be regarded as the qualitative assessment of NPs uptake by cells. Fig. 8(a–c) shows the remarkably visible green fluorescence images with emission wavelength in the range of 500 to 570 nm. In comparison, the weak red fluorescence image with the emission wavelength above 600 nm can be viewed in Fig. S3(a–c).† The bright green intracellular fluorescence can be observed clearly under irradiation of 980 nm wavelength. The corresponding emission spectra has been displayed in Fig. 3(a). The bright field images shown in Fig. 8(b) and the fluorescence images superimposed on the bright field shown in Fig. 8(c) suggest that the cells were

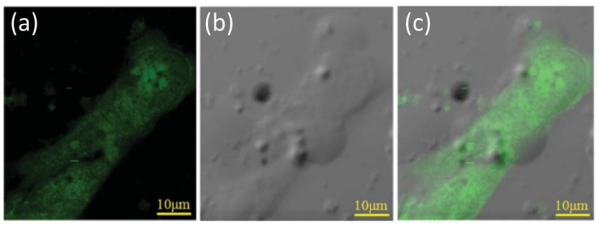

Fig. 8 Confocal laser microscope images of HeLa cells incubated with hollow structured Gd_2O_3 : Ho^{3+}/Yb^{3+} NPs. (a) Fluorescence images under irradiation of 980 nm wavelength with green emission channel. (b) Bright-field image. (c) Super imposed image.

viable without any significant damage and that the Gd_2O_3 : Ho^{3+}/Yb^{3+} NPs were swallowed by the cells and still retained the intrinsic fluorescence.

Furthermore, the superimposed images demonstrates that the green luminescence can be clearly observed in the cytoplasm and the membrane surface of the cells with the luminescence emission originating from various locations across the cell. Heterogeneously distributed luminescence spots observed in the superimposed images are characteristic of the cells exposed to the NPs, which is attributed to the uneven distribution of the luminescence NPs across the intracellular region. These results demonstrate that the visible green fluorescence of the hollow-structured Gd_2O_3 : Ho^{3+}/Yb^{3+} NPs is intense enough for in-cell optical imaging and indicate the great potential for use as fluorescence nanoprobe *in vivo* biotracking and bioimaging due to the successful cellular internalization and bright intracellular luminescence.

To evaluate the cytotoxicity of the hybrid Gd_2O_3 : Ho^{3+}/Yb^{3+} NPs, the CCK-8 assay was undertaken on *in vitro* cell line as a preliminary study of the biocompatibility for imaging applications. The normal embryonic kidney 293 cells and cervical carcinoma HeLa cells were selected to incubate with the NPs at various concentrations for ~10 h and tested the viability using the water-soluble tetrazolium salt WST-8 which is similar and more efficient than MTT agents. Assuming that the viability of the negative control cells was 100% as shown in Fig. 9, the normalized relative viability of the normal embryonic kidney 293 cell line was estimated to be 104.7%, 95.8%, 90.3%, after 48 h at a concentration of 10, 100, 200 μg ml^{-1}, and that of the cervical carcinoma HeLa cell line was 105%, 108.2%, 107.2%, respectively. Despite the high concentration up to 200 μg ml^{-1} and settling of the NPs onto the cell membranes, both normal embryonic kidney 293 cells and cervical carcinoma HeLa cells exhibit regular viability *versus* controls, which means more than 90% of the normal embryonic kidney 293 cells kept alive and less than 10% of the cervical carcinoma HeLa cells were activated.

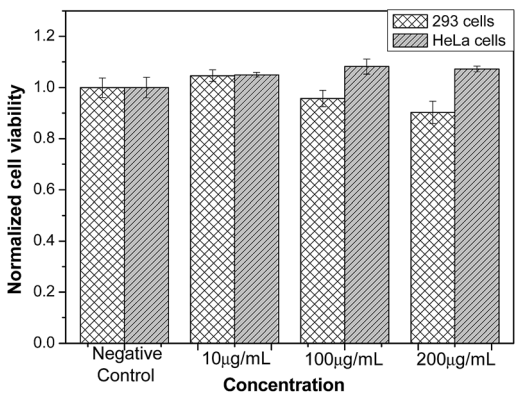

Fig. 9 Normalized cell viability of 293 and HeLa cells after incubation with various concentrations of NPs after 48 h.

The results indicated that the NPs had the low cytotoxicity and would not significantly affected the viability of these two cell types. In general terms, the cytotoxicity of Gd_2O_3-based NPs is mainly originated from the following two cases.[42,43] (1) Free Gd^{3+} ion dissociated from Gd_2O_3 has its intrinsic toxicity which is fatal to cells. (2) Owing to the relatively low water-solubility and the segregation of residual materials, the particle-style agents are easily aggregated and induce the arterial embolism in flowing through capillarism and venules. The NPs possess a unique water-solubility in a relatively low concentration and the outstanding dispersibility as shown in the TEM image. So the toxicity has been speculated primarily originating from the free Gd^{3+}. To explore the probability of Gd^{3+} ions leaking from the NPs, we performed a facile experiment. The as-fabricated NPs with a Gd^{3+} concentration of 1.0 g l^{-1} were dispersed in the presence of 0.9 wt% sodium chloride solution with a running ultrasonic cleaner for 0.5 h, then transferred into a stainless steel sink and stirred for 48 h at 37 °C. After filtrating the aqueous suspension, we determined the concentration of free Gd^{3+} ions in the filtrate with using ICP-AES. The obtained concentration of free Gd^{3+} is 0.023 ppm (0.023 mg l^{-1}) which is extremely low compared to that of the suspension, and the relative leakage ratio is merely 2.3×10^{-5}. Therefore, at a higher dose of toxic free Gd^{3+} ions, there is a certain influence on cell viability. However, the true concentrations utilized in the clinical procedure are extremely low. A previous biological experiment[44,45] with rats shows that no rat dies in the presence of less than 50 mg l^{-1} Gd^{3+} ions and there is no significant deformation of the cells in 14 days if the concentration is less than 10 mg l^{-1}. By contrast, the traditional Cd-containing quantum dot is much higher cytotoxic in spite of a very low dose. These preliminary results indicate that the NPs have extremely low cytotoxicity and exhibit a great potential to be a safe and highly effective contrast agent.

Conclusions

We have successfully fabricated a new bifunctional Gd_2O_3 : RE^{3+}/Yb^{3+} (RE = Er, Ho, Tm) nanocomposite that exhibits highly efficient upconverting luminescence as well as excellent relaxation properties which can be utilized as bimodal imaging agents. The synthesized nanocrystals are spherical and highly monodispersed with a good uniformity and optimum sizes (100–120 nm) for *in vivo* biomedical application. By adjusting the concentration of the sensitizer Yb^{3+} ions, we successfully achieved the highest intensity

of each red (660 nm), green (547 nm) and blue (475 nm) peak for Gd_2O_3 : Er^{3+}/Yb^{3+}, Gd_2O_3 : Ho^{3+}/Yb^{3+} and Gd_2O_3 : Tm^{3+}/Yb^{3+} NPs, respectively. These predominant emissions are generated from the typical f–f transitions of Er^{3+} ($^4F_{9/2}$–$^6I_{9/2}$), Ho^{3+} ($^5F_4$, $^5S_2$–$^5I_8$) and Tm^{3+} ($^1G_4$–$^3H_6$). Our relaxation enhancement strategy for MRI contrast media through constructing a hollow structure achieves an ultrahigh longitudinal relaxivity of 20.53 s^{-1} mM^{-1}, which is attributed to a large number of inner- and outer-surface Gd^{3+} and the efficient chemical exchange between water molecules and Gd^{3+} ions. The live cell bioassays in normal embryonic kidney 293 cells and cervical carcinoma HeLa cells demonstrate that the resulting contrast agents have a great biocompatibility and no observable cytotoxicity at a concentration up to 200 μg ml^{-1}. The outstanding MRI-fluorescent property and low toxicity of the as-formed hollow-structured Gd_2O_3 : RE^{3+}/Yb^{3+} (RE = Er, Ho, Tm) nanoparticles makes it serve as a versatile nanoprobe for magnetic resonance and fluorescence imaging.

Acknowledgements

This study was supported by the National Natural Science Foundation of China (grant no. 11274394), the Fundamental Research Funds for the Central Universities (grant no. 11lgjc12) and the Specialized Research Fund for the Doctoral Program of Higher Education (grant no. 20110171110023).

Notes and references

1 J. Kim, Y. Piao and T. Hyeon, *Chem. Soc. Rev.*, 2009, **38**, 372–390.
2 M. Cho, R. Sethi, J. S. Narayanan, S. S. Lee, D. N. Benoit, N. Taheri, P. Decuzzi and V. L. Colvin, *Nanoscale*, 2014, **6**, 13637–13645.
3 R. Weissleder, *Science*, 2006, **312**, 1168–1171.
4 J. Yu, R. Hao, F. G. Sheng, L. L. Xu, G. J. Li and Y. L. Hou, *Nano Res.*, 2012, **5**, 679–694.
5 G. Choy, P. Choyke and S. K. Libutti, *Mol. Imaging*, 2003, **2**, 303–312.
6 A. Louie, *Chem. Rev.*, 2010, **110**, 3146–3195.
7 E. Terreno, D. D. Castelli, A. Viale and S. Aime, *Chem. Rev.*, 2010, **110**, 3019–3042.
8 L. C. Mimun, G. Ajithkumar, M. Pokhrel, B. G. Yust, Z. K. Elliott, F. Pedraza, A. Dhanale, L. Tang, A.-L. Lin, V. P. Dravid and D. K. Sardar, *J. Mater. Chem. B*, 2013, **1**, 5702–5710.
9 J. F. Barry, D. J. McCarron, E. B. Norrgard, M. H. Steinecker and D. DeMille, *Nature*, 2014, **512**, 286–289.
10 C. Wang, L. Cheng and Z. Liu, *Biomaterials*, 2011, **32**, 1110–1120.
11 P. Zrazhevskiy, M. Sena and X. Gao, *Chem. Soc. Rev.*, 2010, **39**, 4326–4354.
12 H. Abdel-Aty, O. Simonetti and M. G. Friedrich, *J. Magn. Reson. Imag.*, 2007, **26**, 452–459.
13 J. Y. Park, M. J. Baek, E. S. Choi, S. Woo, J. H. Kim, T. J. Kim, J. C. Jung, K. S. Chae, Y. Chang and G. H. Lee, *ACS Nano*, 2009, **3**, 3663–3669.
14 K.-W. Hu, F.-Y. Jhang, C.-H. Su and C.-S. Yeh, *J. Mater. Chem.*, 2009, **19**, 2147–2153.
15 C.-C. Huang, T.-Y. Liu, C.-H. Su, Y.-W. Lo, J.-H. Chen and C.-S. Yeh, *Chem. Mater.*, 2008, **20**, 3840–3848.
16 M.-A. Fortin, R. M. Petoral Jr, F. Söderlind, A. Klasson, M. Engström, T. Veres, P.-O. Käll and K. Uvdal, *Nanotechnology*, 2007, **18**, 395501.
17 Y. Dai, A.-P. Zhang, J. You, J.-J. Li, H.-T. Xu and K. Xu, *RSC Adv.*, 2015, **5**, 77204–77210.
18 K.-Y. Ni, Z.-H. Zhao, Z.-J. Zhang, Z.-J. Zhou, L. Yang, L.-R. Wang, H. Ai and J.-H. Gao, *Nanoscale*, 2016, **8**, 3768–3774.
19 T. S. Atabaev, J. H. Lee, D.-W. Han, H.-K. Kim and Y.-H. Hwang, *RSC Adv.*, 2014, **4**, 34343–34349.
20 N.-Q. Luo, C. Yang, X.-M. Tian, J. Xiao, J. Liu, F. Chen, D.-H. Zhang, D.-K. Xu, Y.-L. Zhang, G.-W. Yang, D.-H. Chen and L. Li, *J. Mater. Chem. B*, 2014, **2**, 5891–5897.
21 I. Solomon, *Phys. Rev.*, 1955, **99**, 559–565.
22 N. Bloembergen, *J. Chem. Phys.*, 1957, **27**, 572–573.
23 N. Bloembergen, E. M. Purcell and R. V. Pound, *Phys. Rev.*, 1948, **73**, 679–712.
24 L. O. Morgan and A. W. Nolle, *J. Chem. Phys.*, 1959, **31**, 365–368.
25 P. F. Cox and L. O. Morgan, *J. Am. Chem. Soc.*, 1959, **81**, 6409–6412.
26 R. B. Lauffer, *Chem. Rev.*, 1987, **87**, 901–927.
27 P. Caravan, J. J. Ellison, T. J. McMurry and R. B. Lauffer, *Chem. Rev.*, 1999, **99**, 2293–2352.
28 P. Caravan, *Chem. Soc. Rev.*, 2006, **35**, 512–523.
29 S. Aime, M. Fasano and E. Terreno, *Chem. Soc. Rev.*, 1998, **27**, 19–29.
30 S. Aime, M. Botta and E. Terreno, *Adv. Inorg. Chem.*, 2006, **57**, 173–237.
31 W. Di, J. Li, N. Shirahata, Y. Sakka, M.-G. Willinger and N. Pinna, *Nanoscale*, 2011, **3**, 1263–1269.
32 X.-Y. Kuang, H. Liu, W.-Y. Hu and Y.-Z. Shao, *Dalton Trans.*, 2014, **43**, 12321–12328.
33 X. Gao, Y. Cui, R. M. Levenson, L. W. K. Chung and S. Nie, *Nat. Biotechnol.*, 2004, **22**, 969–976.
34 W. Cai, A. R. Hsu, Z.-B. Li and X. Chen, *Nanoscale Res. Lett.*, 2007, **2**, 265–281.
35 S. Kim, H. E. Pudavar, A. Bonoiu and P. N. Prasad, *Adv. Mater.*, 2007, **19**, 3791–3795.
36 H. Ow, D. R. Larson, M. Srivastava, B. A. Baird, W. W. Webb and U. Wiesner, *Nano Lett.*, 2005, **5**, 113–117.
37 W.-Y. Hu, H. Liu and Y.-Z. Shao, *New J. Chem.*, 2015, **39**, 7363–7371.
38 L. Zhou, Z. Gu, X. Liu, W. Yin, G. Tian, L. Yan, S. Jin, W. Ren, G. Xing, W. Li, X. Chang, Z. Huc and Y. Zhao, *J. Mater. Chem.*, 2012, **22**, 966–974.
39 X. Lim, *Nature News*, 2016, **531**, 26–28.
40 J. Zhou, Q. Liu and F. Li, *Chem. Rev.*, 2015, **116**, 395–464.
41 H. Liu, L. Li, X.-M. Tian, W.-Y. Hu, X.-Y. Kuang and Y.-Z. Shao, *Eur. J. Inorg. Chem.*, 2012, **2012**, 5677–5684.

42 Y.-Z. Shao, X.-M. Tian, W.-Y. Hu, Y.-Y. Zhang, H. Liu, H.-Q. He, Y.-Y. Shen, F.-K. Xie and L. Li, *Biomaterials*, 2012, **33**, 6438–6446.
43 Y.-Z. Shao, L.-Z. Liu, S.-Q. Song, R.-H. Cao, H. Liu, C.-Y. Cui, X. Li, M.-J. Bie and L. Li, *Contrast Media Mol. Imaging*, 2011, **6**, 110–118.
44 A. J. Spencer, S. A. Wilson, J. Batchelor, A. Reid, J. Pees and E. Harpur, *Toxicol. Pathol.*, 1997, **25**, 245–255.
45 J. Marie Caille, B. Lemanceau and B. Bonnemain, *Am. J. Neuroradiol.*, 1983, **4**, 1041–1042.